CO_2 activation on metal- and non-metal-doped goldene sheets: A DFT Study

Kamal Kumar[1], Abhishek Dhasmana[1], Nora H. de Leeuw[2,3], Jost Adam[4,5], Abhishek K. Mishra[1*]

[1]Department of Physics, Applied Science Cluster, UPES, Dehradun, Uttarakhand 248007, India

[2]Department of Chemistry, University of Leeds, Leeds LS2 9JT, UK

[3]Department of Earth Sciences, Utrecht University, 3584 CB Utrecht, The Netherlands

[4]Computational Materials and Photonics, Department of Electrical Engineering and Computer Science (FB 16) and Institute of Physics (FB 10), University of Kassel, Wilhelmshoher Allee 71, 34121 Kassel, Germany

[5]Center for Interdisciplinary Nanostructure Science and Technology, University of Kassel, Heinrich-Plett-Straße 40, 34132 Kassel, Germany

***Corresponding author :** akmishra@ddn.upes.ac.in; mishra_lu@hotmail.com

ABSTRACT

Goldene is a novel two-dimensional monolayer (2D) of gold atoms arranged in a hexagonal close-packed crystal lattice. In this study, we have employed density functional theory (DFT) calculations to investigate CO_2 activation on doped goldene sheets (G_X, where X represents the dopant). We targeted three distinct categories for the doping process: Alkali metals (AMs = Li, Na, K, and Rb), alkaline earth metals (AEMs = Be, Mg, Ca, and Sr), and non-metals (NMs = C, O, and Se). Our study reveals that Be doping leads to the most robust structure among all considered G_X sheets, with a binding energy (E_b) of -4.73 eV, whereas AEM dopants are found to bind more strongly with goldene compared to AM dopants. No dopant was able to induce a gap between the energy bands, and the goldene preserves its metallic character and flat geometry even after doping. The CO_2 molecule adsorbs on AM-doped goldene sheets with a high adsorption energy (E_{ads}) but remains linear after adsorption. However, in the case of AEMs, CO_2 chemically adsorbs on the G_Be sheet and becomes activated by bending (136.28°). The presence of NMs (C and O) enhances the chemical activity of goldene towards CO_2 conversion.

Keywords: Goldene; DFT; CO_2 Activation; Doping

Introduction

Humanity faces an unparalleled challenge from climate change, largely fuelled by the regular growth in anthropogenic carbon dioxide (CO_2) in the atmosphere [1]. To address this threat, advanced innovative strategies are required to mitigate the environmental impacts of CO_2 emissions [2]. Carbon capture and utilization (CCU) is a vital technology for combating the challenges posed by growing carbon emissions [3], providing economically viable and sustainable solutions [3]. The key approach of CCU is the conversion of captured CO_2 into valuable chemicals and fuels, which helps to meet rising energy demands and achieve CO_2 reduction goals [3].

Atomically thin monolayers of two-dimensional (2D) materials have garnered considerable attention because of their exceptional and unique properties [4]. Encouraged by the successful synthesis of graphene, numerous 2D materials have been synthesized and utilized in diverse fields, including catalysis, gas sensing, optoelectronics, and energy [5]. MXenes [6], transition metal dichalcogenides (TMDs)[7], borocarbo nitrides (BCN) [8], and 2D transition metal oxides (TMO), along with their derivatives, with weak interlayer bonding and sheet-like geometry, exhibit high chemical activity and large surface areas when exfoliated [9]. These characteristics lead to superlative magnetic, photonic, and catalytic properties, different from their bulk counterpart, providing impressive advantages in different applications [10].

2D mono-elemental Xenes are a novel category of 2D materials that have gained significant attention after borophene and phosphorene showed exceptional performance in nanotechnology [11]. This distinct class of 2D materials, including silicene [12], stanene, germanene, arsenene [13], antimonene [13], selenene [14], tellurene [15] and bismuthene [16], could be applied to address challenges in healthcare, environment, and electronics [11]. Furthermore, these 2D materials effectively activate the linear CO_2 molecule on their surface and initiate its conversion process [16]. Although there is a plethora of potential applications for these materials, it is essential to engineer them to improve their performance and durability [17], for example through surface functionalization [18], strain engineering [19,20], doping/decoration [21], alloying [22] or defect creation [23], where the selection of a particular engineering technique is based on the nature and application of the material [23]. Among these techniques, doping by foreign atoms is the most fundamental way to modify the active sites, catalytic performance, local electronic distribution, and surface morphology of 2D materials for applications in electrocatalysis [23,24]. Several

theoretical and experimental studies are available in the literature that have evaluated the CO_2 adsorption capacity of doped 2D Xenes and demonstrated that doping can be utilized to enhance the CO_2 uptake of Xenes [10, 17]. These dopants may be alkali metals (AM) [25], alkaline earth metals (AEM) [26], transition metals (TM) [27], or non-metals (NM) [28]. AMs and AEMs possess high electro-positivity, and they donate electrons easily [25, 26]. This electron-donating nature facilitates the interaction and charge transfer between CO_2 and the adsorbent materials, leading to high adsorption energies along with the activation of the linear CO_2 molecule, ready for its electrochemical conversion. Lalitha *et al.* [29] employed density functional theory (DFT) calculations to study the adsorption of H_2, CO_2, NH_3, and CH_4 at pristine and Ca-doped phosphorene [29]. They found that CO_2, H_2, and CH_4 gas molecules are physically adsorbed at pristine phosphorene with binding energies of -0.147, -0.049, and -0.318 eV, respectively, while NH_3 exhibits a maximum adsorption energy of -0.546 eV. When phosphorene is doped with single Ca atoms, the binding energies of CO_2, H_2, CH_4, and NH_3 increase to -2.932, -3.009, -3.956, and -4.875 eV, respectively, showing chemisorption of these gas molecules at the surface of Ca-doped phosphorene [29]. Ebrahimi *et al.* [30] investigated the adsorption behaviour of various gas molecules (CO, H_2S, CO_2, SO_2, and NO_2) at alkali metal (Li, Na, K, Rb, Cs) doped phosphorene [30]. Their study revealed that Li-decorated phosphorene is the most robust sheet and leads to maximum binding energies with the considered gases [30]. A theoretical study by Zhu *et al.* [31] has demonstrated that the presence of Li atoms at the surface of silicene results in high CO_2 storage capacity (-0.19 eV), whereas pristine silicene is not suitable for CO_2 adsorption due to weak-physisorption [30]. Arefi *et al.* [32] studied the effect of adding Na atoms on the CO and CO_2 adsorption characteristics of borophene. The CO and CO_2 molecules were found to bind with pristine borophene with energies of -0.328 eV and -0.490 eV, respectively [32], whereas after decoration with Na atoms, the binding energies of the CO and CO_2 molecules become -1.136 and -0.867 eV [32]. They explained this increase in binding energy by a charge transfer mechanism as they found that the Na atom transfers charge to these molecules owing to its lesser electronegativity compared to the B atoms of borophene [32].

To design an efficient catalyst, Xenes can be doped with various NMs (C, O, N, and Se), which are readily available and inexpensive. Such a catalyst can be operated under harsh reaction conditions of high temperature and pressure [33,34]. These qualities make them promising candidates for the large-scale electrochemical conversion of CO_2 [33,34]. Therefore, along with

AM- and AEM-doped 2D Xenes, the theoretical investigation of NM-doped Xenes for the catalytic conversion of CO_2 becomes essential.

Gold has historic significance owing to its remarkable stability under extreme conditions and oxidation resistance [35]. Although the bulk metal is considered catalytically inactive and chemically inert, its nanoparticles possess outstanding catalytic activity for different chemical reactions [36]. It has been found that the catalytic performance of its nanoparticles is highly sensitive to various factors, such as shape, size, nature of substrate, and physical state of the gold particles [37]. In 2015, Yang and colleagues proposed a highly stable 2D monolayer of gold atoms arranged in a hexagonal close-packed crystal lattice [38]. They studied various planar and buckled crystal lattices of gold, including honeycomb, hexagonal close-packed, square, and tetra-coordinate structures, and they found that the most stable 2D structure for freestanding Au atoms is the planar hexagonal close-packed structure [37]. This 2D monolayer corresponds to the top layer of an Au(111) surface and characterizes a 2D delocalized gas [37]. Wang *et al.* [38] have fabricated monatomic (with a thickness of 0.6 nm) 2D membranes of Au atoms through in-situ de-alloying inside a transmission electron microscope (TEM) [38]. This membrane is highly resilient when exposed to a high-energy beam [38]. In 2023, Kashiwaya *et al*. [39] successfully synthesized a free-standing and single-atom-thick 2D monolayer of Au atoms, named goldene, by wet chemical etching of Ti_3C_2 from Ti_3AuC_2 [39]. They also confirmed the hexagonal close-packed (hexagonal triangular) structure of goldene as suggested by Yang *et al*. [37]. Recently, Shi *et al.* reported the successful isolation of 2D trilayer-thick gold sheets, referred to as trilayer goldene. These sheets have a thickness of approximately 6.7 Å and were synthesized through selective etching of Ti_4C_3 from the newly formed MAX phase $Ti_4Au_3C_3$. The parent compound is created by thermally annealing Au-capped Ti_4SiC_3 thin films, where gold completely replaces silicon [40]. Furthermore, Shun *et al.* demonstrated the exfoliation of single-atom-thick gold layers, referred to as goldene, through a wet-chemical etching process that removes Ti_3C_2 from the nano-laminated precursor Ti_3AuC_2. This precursor is synthesized by substituting silicon (Si) with gold (Au) in the well-known MAX phase Ti_3SiC_2. The method employed is straightforward, scalable, and notably free of hydrofluoric acid, offering a safer approach to synthesizing two-dimensional gold [41].

Our earlier theoretical study based on DFT has shown that the CO_2 molecule interacts physically with a pristine goldene monolayer with an adsorption energy of -0.27 eV [42]. This physisorption

of CO_2 at goldene remains consistent in the presence of mono-, di-, and tri-vacancies with adsorption energies of -0.27 eV, -0.26 eV, and -0.32 eV, respectively [42]. However, when goldene is doped with N (n-type doping) and B (p-type doping) atoms, CO_2 adsorbs chemically and is activated, with a negative Bader charge transfer [40]. The adsorption energies of CO_2 at N- and B-doped goldene increase up to -1.70 eV and -1.44 eV, respectively [42].

Recent breakthroughs in two-dimensional materials, such as graphene and molybdenum disulfide (MoS_2), have compellingly demonstrated the potential for incorporating alkali, alkaline-earth, and non-metal dopants. This research paves the way for innovative doping strategies in goldene materials, enhancing their properties and applications. Ullah *et al.* reported controllable p-type doping of monolayer MoS_2 via sodium (Na) intercalation during the chemical vapor deposition (CVD) process. X-ray techniques confirmed the incorporation of sodium (Na) into the MoS_2 lattice, resulting in p-type carrier conduction. Additionally, the photo response of the MoS_2 photodetector improved approximately twofold compared to a pristine MoS_2 photodetector, indicating enhanced optoelectronic properties [43]. The experimental study of Marchianai *et al.* demonstrated potassium (K) intercalation into few-layer graphene (FLG), achieved through deposition in ultra-high vacuum conditions. This process resulted in significant changes in the electronic properties of graphene, including increased conductivity and the emergence of n-type behavior [44].Chapman *et al.* experimentally demonstrated that the intercalation of calcium (Ca) in graphene laminates induces superconductivity at temperatures of around 6 K. The study found that Ca is the only dopant among several tested (including potassium, cesium, and lithium) that induces superconductivity in graphene laminates. The transition temperature was found to be strongly dependent on the confinement of the Ca layer and the induced charge carrier concentration [45]. CO_2 activation is a fundamental criterion for any electrocatalyst. This study focuses on identifying doped goldene systems capable of activating CO_2, thus providing a basis for further investigations into complete CO_2 reduction pathways. In this study, we have continued our study of CO_2 adsorption at goldene, here investigating metal- (AM and AEM) and non-metal-doped goldene monolayers (G_X, X= Li, Na, K, Rb, Be, Mg, Ca, Sr, C, O, and Se) through first-principles calculations based on DFT. We confirm the nature of the interaction and activation of the CO_2 molecule at G_X by projected density of states (PDOS), electronic band structure (EBS), Bader charge transfer between CO_2 and G_X, charge density difference, and work function plots.

2. Computational Details

All the calculations performed in this study are conducted with the Quantum Espresso (QE) [46] simulation package based on the density functional theory (DFT) [47]. The generalized gradient approximation (GGA) [48] in the form of the Perdew-Burke-Ernzerhof (PBE) [49] functional is utilized for the approximation of the exchange-correlation functional. The projected augmented wave (PAW) [50,51] approach is used to treat the interaction between electrons and ions and describe the behaviour of core and valence electrons. The Grimme-D3 [52] method is incorporated to include long-range interactions and Van der Waals correction, which improves the accuracy of dispersion forces between molecules and distinct atoms.

The freestanding goldene is modelled by a 5×5×1 supercell, which comprises 25 Au atoms. A vacuum of 12 Å is applied perpendicular to the plane of the goldene supercell (in the z-direction) to avoid interactions between the periodic images of repeated cells. Integration of the Brillouin zone is carried out by a Monkhorst-Pack grid of 9×9×1 for structural optimization and relaxation and 18×18×1 for density-of-states (DOS) calculations. A well-converged cut-off energy of 570 eV is applied in all calculations, and full relaxation of the structures is deemed to have been achieved when the residual force on individual ions is less than 0.01 eV/ Å. The amount of charge transfer between CO_2 and different goldene sheets is obtained by the Bader charge transfer method [53]. The binding energies (E_b) [54] of different dopants with the goldene monolayer, cohesive energy (E_c) [55], and the adsorption energies (E_{ads}) [56] of the CO_2 molecule at various doped goldene sheets are calculated by equations (i), (ii), and (iii), respectively.

$$E_b = E_{sheet+X} - E_{sheet} - E_X \quad \text{(i)}$$

$$E_c = \frac{E_{sheet+X} - n1(E_{Au}) - n2(E_X)}{n} \quad \text{(ii)}$$

$$E_{ads} = E_{sheet+X+CO2} - E_{sheet+X} - E_{CO2} \quad \text{(iii)}$$

where $E_{sheet+X+CO2}$, $E_{sheet+X,}$ and E_{sheet} are the total energies of the system with CO_2 adsorbed at G_X sheets, G_X sheets, and pristine goldene sheets, respectively.

E_X, E_{Au}, and E_{CO2} are the total energies of the X atom, Au atom, and isolated CO_2 molecule, respectively. n1 and n2 represents total number of Au and X atoms and n is the total number of atoms in the sheet.

The work function (W), which is defined as the difference between the vacuum and Fermi energy, is calculated by equation (iv) [57].

$$W = \phi_{vac} - E_f \quad \text{(iv)}$$

Where, ϕ_{vac} and E_f represent the vacuum and Fermi energy, respectively.

3. Results and Discussion

Goldene is a 2D planar monolayer with one Au atom in its unit cell and the Hexagonal P6/mmm (#191) space group as shown in **Figure 1**. The optimized cell parameters (a = b = 2.74 Å) are found to be in good agreement with earlier theoretical [37] as well as experimental results [39]. The average Au-Au bond length and in-plane bond angle are 2.73 Å and 60°, respectively. In order to obtain insights into the distribution of atomic orbitals and energy levels, we have plotted the projected density of states (PDOS) and electronic band structure (EBS) of the goldene monolayer (**Figure S1** of the supplementary file). Our plotted PDOS and EBS profiles agree well with the plots of Yang et al. [37]. From **Figure S1**, it is clear that pristine goldene shows metallic behaviour as no energy gap is found in the PDOS between the valence band (VB) and conduction band (CB) near the Fermi level (E_f). In the EBS, one energy level of a nearly free electron crosses E_f midway, which signifies that electrons from the VB are donated to the free electron gas. Thus, akin to bulk Au, the 2D monolayer of Au also possesses diamagnetic and metallic behaviour. In PDOS, the major contribution in the VB arises from the d-orbital of the Au atom, while s- and p-orbitals contribute equally near E_f. **Figure 1** represents the crystal structure of a 2D goldene monolayer and the dopant site considered for the doping by various Ams, AEMs, and NMs dopants

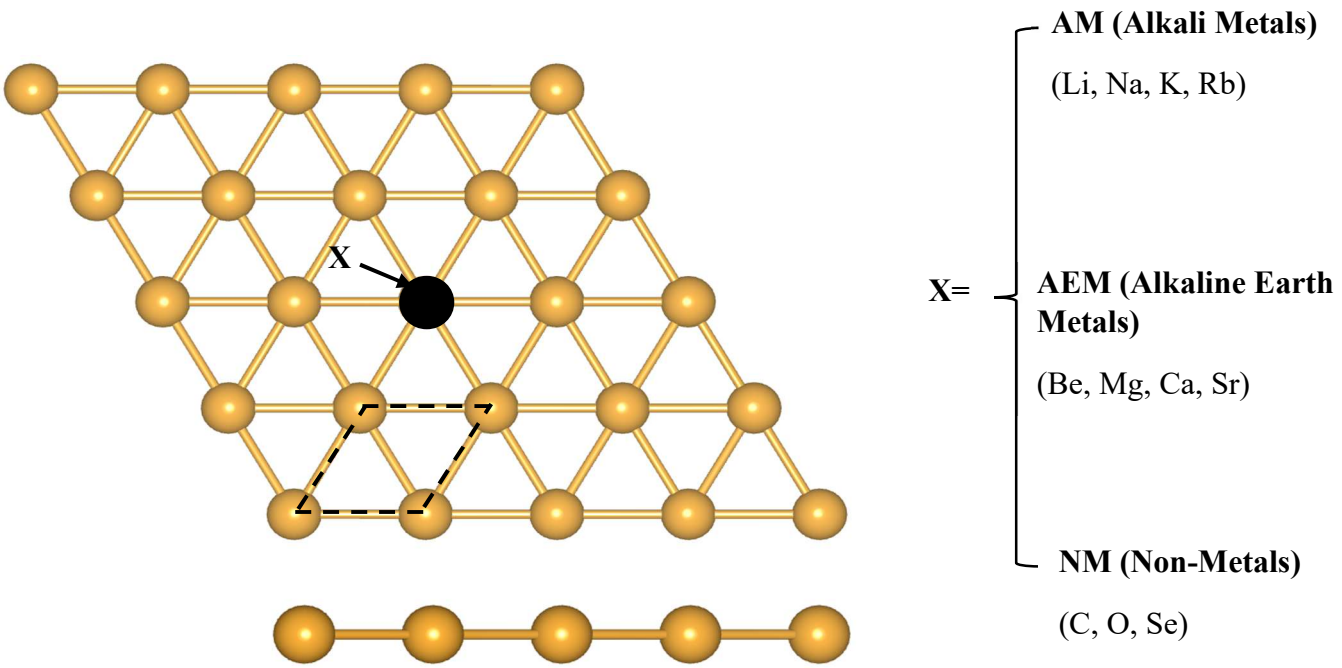

Figure 1 Schematic (top and side view) of 551 supercell of goldene with different dopants (AMs, AEMs and NMs). Au atoms in 2D goldene monolayer are arranged in planar hexagonal closed packed (triangular) crystal lattice. Black rhombus (in dotted line) represents the unit cell of goldene monolayer which contains one Au atom. Yellow spherical balls represent Au atoms.

3.1 X-doped goldene (G_x)

In this section, we discuss the structural and electronic properties of various doped goldene sheets (G_X). To design G_X sheets, one Au atom from the middle of the goldene supercell is replaced by an X atom (**Figure 1**). The relaxed geometries of various G_X sheets are shown in **Figure 2**. The binding energies along with Bader charge transfer onto the X atoms, as well as the relaxed Au-Au and Au-X bond lengths of all considered sheets, are summarized in **Table 1**. For AM dopants (Li, Na, K and Rb), the maximum E_b is found for the Li atom at -3.94 eV with a Bader charge transfer of 0.86 e^- and both relaxed Au-Au and Au-Li bond lengths of 2.69 Å, whereas the E_b for Na, K and Rb atoms are -2.74, -1.42 and -0.75 eV, respectively (**Table 1**). Thus, the Li atom forms the most robust chemical bond with the Au atoms of goldene, whereas the Rb atom is bound most weakly among all the AM dopants. As a result, the Au-X bond length is longest for Rb (2.86 Å)

and shortest for Li (2.69 Å) dopants. After doping with the Rb atom, the Au-Au bond length of goldene also elongates from 2.74 Å to 2.87 Å.

The order of E_b for the AEM dopants is Be (-4.73 eV) > Ca (-4.69 eV) > Mg (-4.33 eV) > Sr (-3.79 eV) (**Table 1**). Comparison between the G_{Li} and G_{Be} sheets shows that G_{Li} is more stable. Furthermore, the introduction of Be atom in goldene causes a contraction of 3.65% in Au-Au spacing. Although Sr (-3.79 eV) exhibits the lowest E_b in the AEM series, even this value is five times higher than the E_b of Rb, which possesses the lowest E_b in the AM category. If we exclude Sr, E_b of all AEM dopants is higher than the E_b of Li. Thus, AEM-doped goldene sheets are more energetically stable than of AM-doped goldene sheets. The negative sign of E_b indicates that all dopants form stable chemical bonds with the goldene monolayer and the doping process of goldene with AEM dopants is thermodynamically favourable. Owing to the lower electronegativity of AMs and AEMs compared to Au, they lose electrons and gain a positive Bader charge, while the goldene monolayer acts as an electron acceptor (**Figure 3**). The donated electrons from the AEMs and AMs are populated in the conduction band (CB), which do not, however, change the existing distribution of energy levels in the EBS, and the goldene monolayer therefore remains metallic. AEMs are more electronegative than AMs owing to their higher ionisation potential. Since the ionization energy and electronegativity decrease as the atomic radius increases down the group in the periodic table, their ability to donate electrons is enhanced. As a result, the work function (W), defined as the minimum energy required to remove an electron from the material's surface, also decreases. As such, G_{Li} and G_{Be} sheets exhibit the highest W (5.42 eV and 5.34 eV, respectively) among the considered AM and AEM dopants.

In contrast, all NMs act as electron acceptors owing to their higher electronegativity, and they become negatively charged after doping in the goldene monolayer. In the PDOS (**Figure 4**) of the G_{NM} sheet, a small peak of a p-orbital arises near E_f, which confirms hybridization of the p-orbital of the NMs with the s-orbital of the Au atoms of the goldene monolayer. However, this hybridization does not cause significant asymmetry in the PDOS near the E_f and is unable to create a gap between VBs and CBs (**Figure S2**). Even after doping of AMs, AEMs, and NMs, the goldene monolayer remains flat without evidence of buckling. The E_b of C, O, and Se NMs with the pristine goldene are -4.02, -3.89, and -4.42 eV, respectively. The higher E_b of the C atom than O is due to the formation of a covalent bond between the Au and C atoms, whereas the nature of the Au-O

bond in the Au/O sheet is partially ionic due to the formation of the metal-oxygen bond. O is more electronegative than C and attracts more (-0.70 e^-) electron density than the C atom (-0.24 e^-). The Se atom forms the strongest covalent bond with the Au atoms of goldene among the NMs. Furthermore, the large atomic radius of the Se atom compared to the O and C atoms leads to the Se atom possessing a better spatial fit with pristine goldene leading to a high E_b (-4.42 eV) and stable interaction. The relaxed Au-Au and Au-Se bond lengths are 2.74 Å in G_{Se} sheet, which is similar to pristine goldene, and the Se dopant atom fits well into the goldene monolayer without causing elongation or contraction in the Au-Au bond length (**Table 1**). The calculated W of the G_{C}, G_{O}, and G_{Se} sheets are 5.45, 5.63 and 5.49 eV, respectively.

The calculated cohesive energy E_c values for all doped goldene systems lie between −2.87 and −3.03 eV/atom, indicating that the doped sheets are thermodynamically stable. Such large negative E_c values confirm the strong binding of dopant atoms with the Au lattice, preventing dopant segregation and ensuring the robustness of the modified monolayers. Among the studied dopants, alkaline earth metals generally exhibit slightly more negative E_c values, reflecting their stronger interaction with the goldene compared to AMs and NMs.

The lattice deformation induced by doping in the goldene sheet was quantified by the deformation energy (E_{def}). Alkali dopants show a size-driven increase, Li→Rb: 0.003→0.64 eV, consistent with local Au–Au ring expansion (d_1 up to ~2.87 Å) and longer Au–X bonds. In the alkaline-earth series, deformation remains low for small ions (Be 0.04, Mg 0.03 eV) but rises for larger Ca (0.21) and Sr (0.46 eV), reflecting increasing size mismatch. Non-metal dopants (C, O, Se) yield negligible E_{def} (0.01–0.07 eV) and minor bond adjustments, indicating the lattice largely preserves its framework with only localized distortions around the dopant.

The calculated work function (W) of pristine goldene was found to be 5.48 eV. The W values for all doped configurations are reported in **Table 2**. AM dopants, particularly K (5.16 eV) and Rb (5.06 eV), as well as heavier AEM dopants Ca (5.07 eV) and Sr (4.97 eV), markedly reduce the W relative to the pristine sheet, indicating increased surface electron density and a tendency to donate electrons to adsorbates. In contrast, electronegative dopants such as O increase W to 5.63 eV, reflecting electron depletion from the surface.

Table 1. Calculated binding energies E_b (eV), cohesive energies E_c (eV/atom), deformation energy E_{def} (eV), bond lengths d_1 and d_2 (Å), Bader charge transfers Δq_x and work functions W(eV) of the different G_X sheets.

Dopant	X	E_b	E_c	E_{def}	d_1 (Au-Au)	d_2 (Au-X)	Δq_x	W
AM	**Li**	-3.94	-2.99	0.003	2.69	2.69	0.86	5.42
	Na	-2.74	-2.95	0.11	2.75	2.76	0.77	5.38
	K	-1.42	-2.89	0.44	2.84	2.83	0.71	5.16
	Rb	-0.75	-2.87	0.64	2.87	2.86	0.72	5.06
AEM	**Be**	-4.73	-3.03	0.04	2.64	2.64	1.95	5.34
	Mg	-4.33	-3.01	0.03	2.73	2.72	1.54	5.23
	Ca	-4.69	-3.02	0.21	2.78	2.79	1.38	5.07
	Sr	-3.79	-2.99	0.46	2.83	2.84	1.37	4.97
NM	**C**	-4.02	-3.00	0.02	2.66	2.65	-0.24	5.45
	O	-3.89	-2.99	0.01	2.68	2.68	-0.70	5.63
	Se	-4.42	-3.01	0.07	2.74	2.74	-0.12	5.49

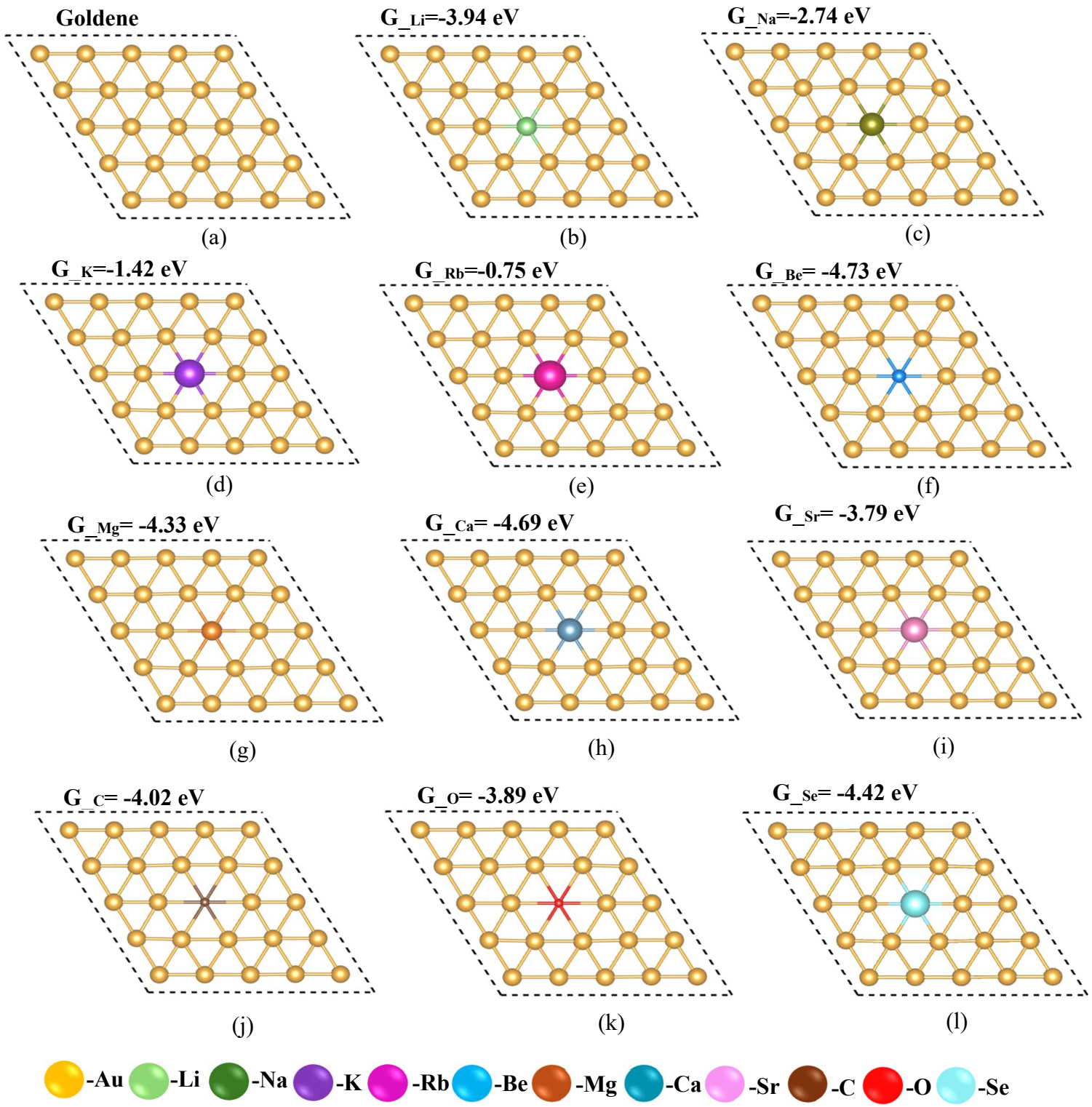

Figure 2 Relaxed geometries of (a) pristine goldene sheet and sheets doped with AMs (b) Li, (c) Na, (d) K; AEMs (e) Rb, (f) Be, (g) Mg, (h) Ca, (i) Sr; and NM (j) C, (k) O, (l) Se, showing the binding energies of different dopants. G_{Be} is the most robust structure among the G_X sheets.

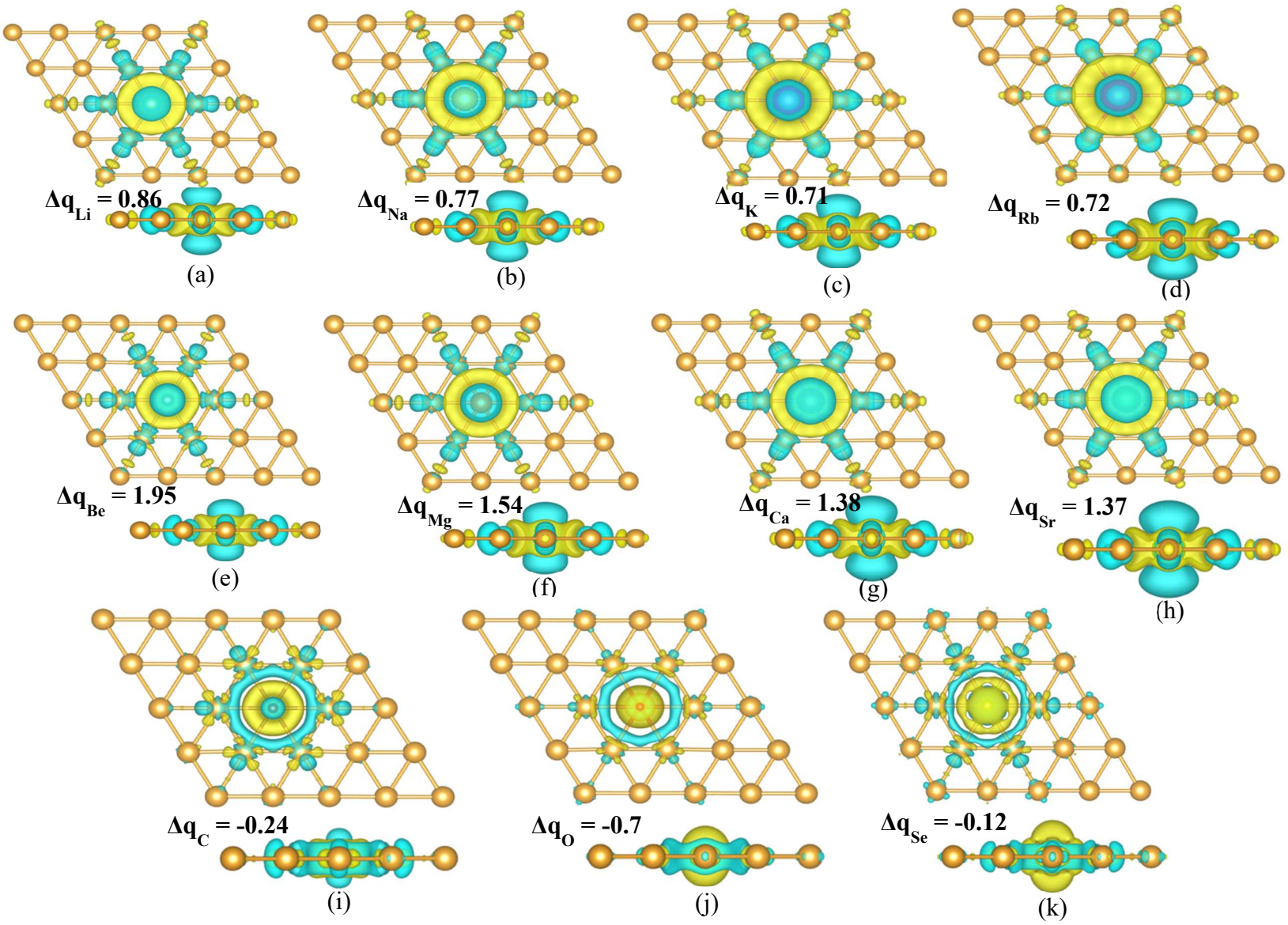

Figure 3 Charge density difference and Bader charge transfers at goldene sheets doped with AMs (a) Li, (b) Na, (c) K; AEMs (d) Rb, (e) Be, (f) Mg, (g) Ca, (h) Sr; and NMs (i) C, (j) O, (k) Se. AMs and AEMs act as electron donors, while NMs act as electron acceptors.

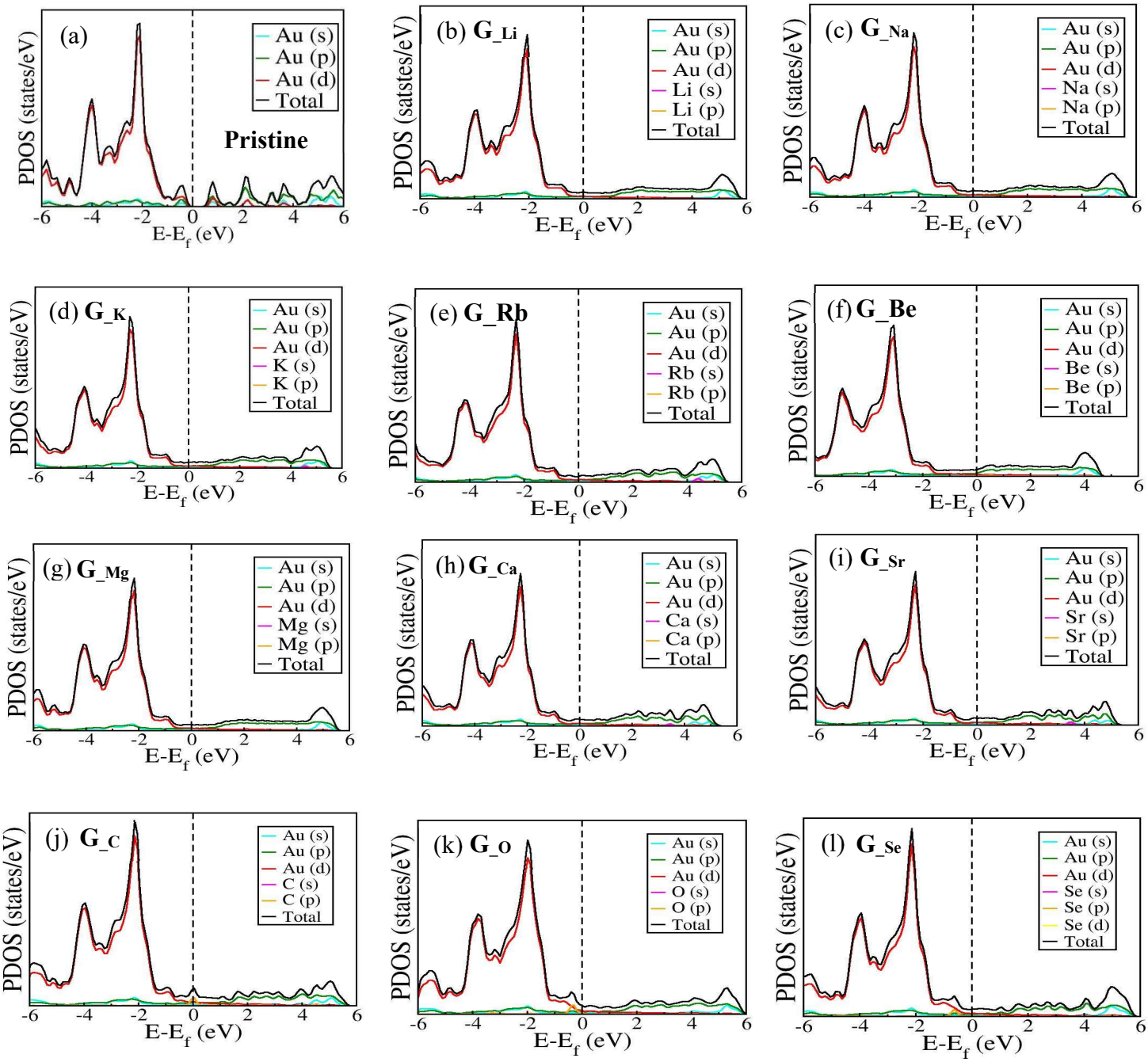

Figure 4 PDOS of (a) pristine goldene sheet and sheets doped with AMs (b) Li, (c) Na, (d) K; AEMs (e) Rb, (f) Be, (g) Mg, (h) Ca, (i) Sr; and NMs (j) C, (k) O, (l) Se. All $G_{\_X}$ sheets are found to be metallic in nature

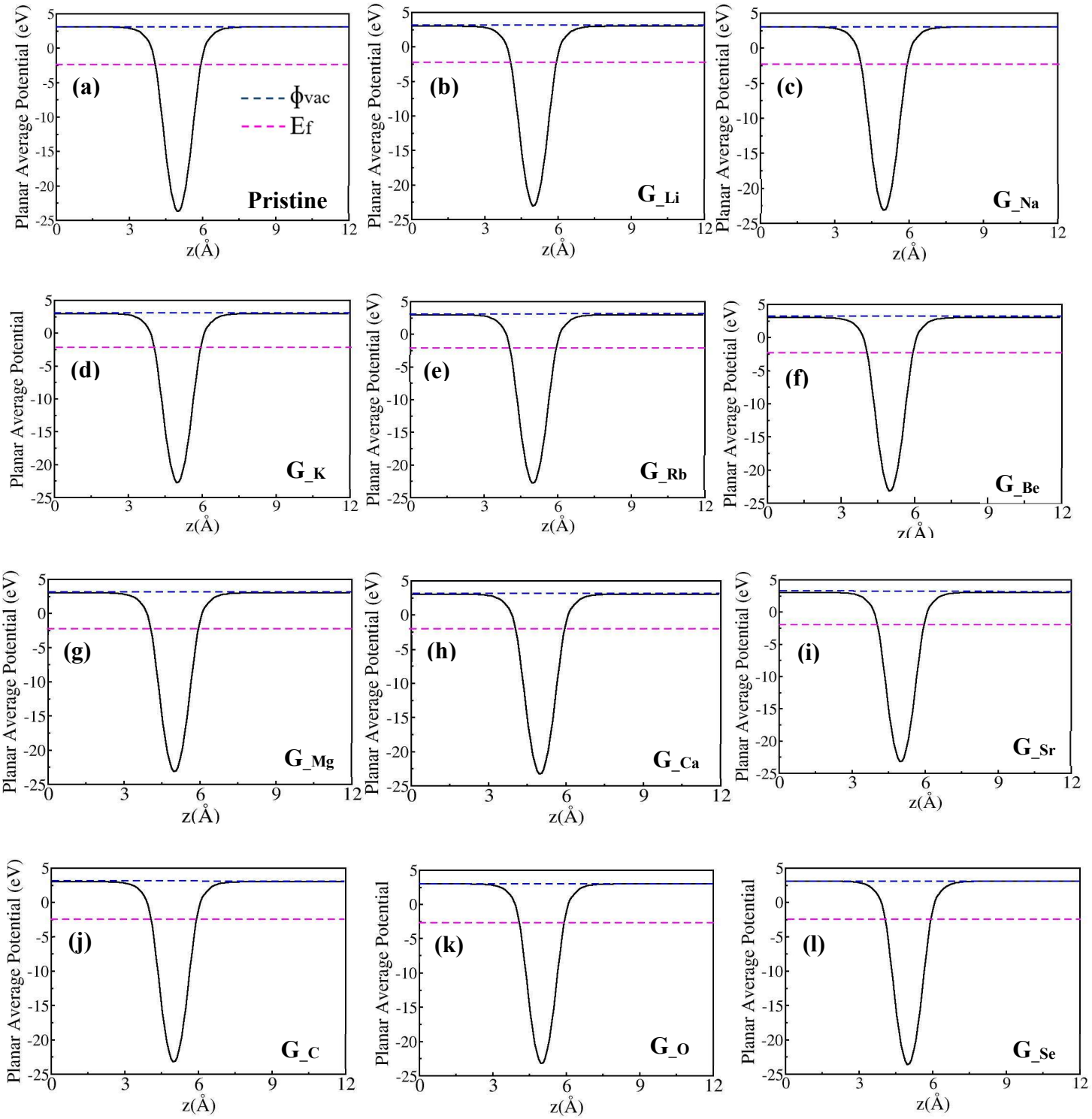

Figure 5 Work functions of (a) pristine goldene sheet and sheets doped with AMs (b) Li, (c) Na, (d) K; AEMs (e) Rb, (f) Be, (g) Mg, (h) Ca, (i) Sr; and NMs (j) C, (k) O, (l) Se. Blue and magenta dotted lines represent vacuum level and Fermi energies, respectively.

3.2 CO_2 adsorption at X-doped goldene (CO_2+G_X)

In this section, we discuss the adsorption of a CO_2 molecule on different X-doped goldene sheets. The adsorption was studied by placing a CO_2 molecule in different configurations and alignments at all possible adsorption sites (**Figure S3-S5**). The key configurations included placing the C or O atom of the CO_2 molecule above an X atom or between the dopant X and neighbouring Au atoms. All of these structures were fully relaxed to obtain the most favourable configuration of CO_2 at the G_X sheets. The calculated adsorption energy E_{ads} (eV), adsorption height h (Å), optimized bond lengths d (Å), bond angle θ (°), and Bader charge transfer Δq_{co2} for the most stable configurations are summarized in **Table 2**.

Table 2: Adsorption energy E_{ads} (eV), deformation energy E_{def} (eV), adsorption height h (Å), bond lengths d_1, d_2, d_3 and d_4 (Å), work function W(eV), , CO_2 bond angle θ (), and Bader charge transfer on dopants Δq_X and most stable CO_2 configurations Δq_{CO_2} on different doped goldene sheets

Sheets	E_{ads} (eV)	E_{def} (eV)	h	d_1 (Au-Au)	d_2 (Au-X)	d_3 (C-O)	d_4 (X-O)	θ	Δq_X	Δq_{CO_2}	W
G_Li	-0.42	-0.007	3.98	2.68	2.82	1.17	1.99, 4.33	179.99	0.88	-0.006	5.34
G_Na	-0.82	-0.58	3.01	2.69	3.09	1.17	4.54, 4.54	179.99	0.85	-0.02	5.17
G_K	-2.29	-2.04	3.00	2.68	3.47	1.17	5.17, 5.17	179.98	0.86	-0.03	5.01
G_Rb	-2.96	-2.72	3.03	2.68	3.61	1.17	5.41, 5.42	179.99	0.86	-0.03	4.99
G_Be	-0.37	0.55	2.49	2.69	3.13	1.23	1.39, 2.45	136.28	1.95	-0.67	5.54
G_Mg	-0.43	0.07	3.09	2.71	2.73	1.16	2.18, 3.16	178.46	1.56	-0.03	5.20
G_Ca	-0.84	-0.61	3.47	2.70	2.98	1.17	4.11, 4.50	179.30	1.46	-0.03	4.96

G_Sr	-1.66	-1.42	3.12	2.70	3.13	1.17	4.64, 4.64	179.36	1.49	-0.03	4.86
G_C	-1.84	-0.72	1.28	2.71	4.13	1.38	1.19, 1.51	136.79	0.09	-0.41	5.64
G_O	-1.18	0.003	1.36	2.91	3.42	1.27	1.82, 1.82	122.83	-1.55	0.49	5.82
G_Se	-0.26	-0.01	3.04	2.73	2.78	1.17	3.62, 3.62	179.56	-0.11	-0.03	5.45

After relaxation, the most stable configuration of the CO_2 molecule at the Li-doped goldene sheet was found when CO_2 was positioned directly above the Li atom in a vertical alignment, where the molecule undergoes strong physical adsorption with E_{a_Li} of -0.42 eV (**Figure 6**). After relaxation, a bond of 1.99 Å is formed between the Li dopant and the O atom of the adsorbed CO_2, as shown in **Figure 6**. The strong Van der Waals interaction between CO_2 and G_Li pulls the Li atom upwards, and the Au-Li bond length increases from 2.69 Å to 2.82 Å (**Figure 6**). The outermost s and p orbitals of the Li and O atoms overlap and the Li atom becomes more positive as it transfers electron density to the O atoms of the CO_2 molecule (**Figure 7 and 8**), which leads to the formation of a sigma bond (polar covalent bond) between the Li and O atoms.

In contrast to the Li-doped goldene, for the other G_AM sheets, the maximum E_{a_AM} is found when the CO_2 molecule is placed horizontally (parallel to the doped goldene sheets) above the doped AMs. For the Na-doped goldene sheet, we found E_{a_Na} to be -0.82 eV, reflecting strong physisorption. As seen on all AM-doped goldene sheets, the geometry of the adsorbed CO_2 molecule remained linear, with a C-O bond length of 1.17 Å. The CO_2 molecule bound to the surface of the G_K sheet with an energy of -2.29 eV at a height of 3.00 Å due to a negative charge transfer of $-0.03e^-$. Since among the G_AM sheets G_Rb possesses the lowest W, it promotes the charge transfer mechanism between CO_2 and the G_Rb sheet, leading to an E_{ads} of -2.96 eV. Thus, the maximum interaction of CO_2 among all the G_AM sheets takes place at the G_Rb sheet owing to the negative charge transfer (**Figure 7**) of $-0.03e^-$. After adsorption, the doped Na, K, and Rb

atoms are pushed away from the plane of the goldene monolayer due to the interaction with the adsorbed CO_2 molecule, causing an increase in Au-Na, Au-K, and Au-Rb bond lengths by 0.33, 0.64, and 0.75 Å, respectively. The Au-Rb bond has lengthened most owing to the strongest interaction energy E_{a_AM} of CO_2 with the G_{Rb} sheet, leading to greater distortion of the G_{Rb} lattice.

When goldene is doped with AEMs, the highest binding strength of CO_2 with the G_{AEM} sheet (Be, Mg, and Ca dopants) is found when the CO_2 molecule is placed horizontally, with one O atom of the CO_2 positioned above the AEM dopant and the other O atom located above the nearby Au atom of the goldene sheet. The Be atom activates the CO_2 molecule, where, after activation, the C-O bond has elongated from 1.17 Å to 1.23 Å and the molecule is bent to 136.28°. During the adsorption process, the CO_2 molecule acts as an electron acceptor owing to the high electronegativity of the O atoms, and a Bader charge of -0.67e^- accumulates on the molecule. This negative charge further confirms the reduction of CO_2 at the surface of the Be-doped goldene sheet. As we move down any column in the periodic table, the polarizability of the elements increases due to their increasing atomic size, leading to diffuse electron clouds. This increase in polarizability also promotes the CO_2-G_{AEM} interaction, as orbitals overlap and cause dipole-dipole interactions. This trend results in a progressive increase in E_{a_AEM} of the CO_2 adsorbing at G_{Mg} (-0.43 eV), G_{Ca} (-0.84 eV), and G_{Sr} (-1.66 eV) sheets. The Bader charge transfer to CO_2 for the G_{Mg}, $G\text{-}_{Ca,}$ and G_{Sr} sheets remains almost constant (-0.03 e^-), which suggests that the binding of the CO_2 molecule to these sheets predominantly arises due to the physical interactions rather than chemical interactions. The strong interaction between CO_2 and $G\text{-}_{Sr}$ creates out-of-plane shifting of the Sr dopant atom, leading to an elongation by 0.29 Å of the Au-Sr bond length.“Thus, in the AEM dopants, only Be-doped goldene uniquely activates CO_2, as evidenced by significant bending (θ = 136.28°) and high charge transfer (Δq_{CO_2} = –0.67 e^-). This arises from small ionic radius and high charge density of Be atom, which create a strong local field and enhance interaction with CO_2, leading to its activation. In contrast, Mg, Ca, and Sr doped goldene sheets exhibit minimal structural distortion and charge transfer, consistent with weak, physisorption-dominated binding.”

When the CO_2 molecule is placed above the G_{NM} sheets, G_{C} and G_{O} successfully activate the CO_2 molecule with E_{a_C} and E_{a_O} of -1.84 eV and -1.18 eV, respectively. When the CO_2 molecule

binds with G_C, it acts as an electron acceptor (-0.41 e^-) due to the high electronegativity of the O atom compared to the C dopant atom, where the G_C behaves as an electron donor. In contrast, electron-rich CO_2 acts as an electron donor when adsorbed at the G-O sheet. The bond angles of the linear CO_2 molecules bend to 136.79° and 122.83° at the G_C and G_O sheets, respectively. The relaxed C-O bond lengths of the CO_2 molecule expand from 1.17 Å to 1.38 and 1.27 Å at G_C and G_O sheets, respectively. Thus, reduction of CO_2 takes place at the surface of the G_C sheet, which is a critical step in the catalytic conversion of CO_2 into valuable chemicals and fuels, whereas, the oxidation of CO_2 at the G_O surface is beneficial for those applications that require milder binding of the CO_2 molecule, such as storage, separation and reversible capture in traditional carbon capture and storage (CCS) technologies.

As discussed in section 3.1, Se-doping of the goldene sheet results in the Se atom possessing similar structural parameters to those of the Au atom in the goldene monolayer. This similarity is further confirmed by the adsorption of the CO_2 molecule at the G_Se sheet, which becomes physiosorbed at the surface of the G_Se sheet, similar to its adsorption on pristine goldene. The E_{a_Se} of CO_2 at G_Se is -0.26 eV, which is only 0.004 eV higher than its adsorption energy at the pristine goldene monolayer [42]. This minor difference in energy arises due to a small transfer of electron density from the doped Se atom to the adsorbed CO_2 molecule. The Bader charge of the CO_2 molecule and adsorption height at G_Se are also similar to its adsorption at pristine goldene.

In all stable configurations of the CO_2 molecule at various G_X sheets, the flat geometry of goldene and its metallic nature (**Figure S6**) remain consistent. The adsorption characteristics of all studied CO_2 configurations at the G_X sheets are summarized in **Table S1**. **Figure 9** shows the calculated work functions of the doped goldene sheets after adsorption of CO_2. The W of G_C and G_O sheets with adsorbed CO_2 are 5.64 and 5.82 eV, respectively, i.e., higher than before CO_2 adsorption (5.45 and 5.63 eV, respectively). This increase in W for both systems suggests a lowering of the Fermi level due to the redistribution of electrons and the creation of surface dipoles aligned with their negative ends towards the vacuum region.

From E_{def} after CO_2 adsorption, it is clear that AM dopants (K and Rb) exhibit the largest structural response, with strongly negative E_{def} values ranging from −2.0 to −2.7 eV, elongated Au–X bonds ($d_2 \approx 3.5$–3.6 Å), and increased adsorption heights ($h \approx 3.0$ Å). These changes indicate that the dopant K and Rb atoms are displaced outward from the goldene sheet after CO_2 adsorption. This

leads to notable local lattice reconstruction, even though the CO_2 molecule remains almost linear, suggesting low activation. On the other hand, AEM dopants (Ca and Sr) show smaller E_{def} and moderate bond elongation, implying weaker structural perturbation. In contrast, Be, despite a moderate positive E_{def} (~0.55 eV), induces pronounced CO_2 bending, implying strong activation with limited lattice penalty. Mg behaves similarly to Ca and Sr with minimal distortion. For non-metallic dopants (C and O), E_{def} values are small, adsorption heights are short (~1.3 Å), and CO_2 bending is significant, which indicates that activation is driven predominantly by electronic interactions with only localized lattice deformation.

For G_{Rb} goldene sheet, E_{ads} is calculated to be –2.96 eV, which is higher than in the G_{Be}, G_{C}, and G_{O} sheets. Despite this strong binding, Bader charge analysis indicates that CO_2 gains only –0.03 e^- upon adsorption, suggesting negligible electron transfer to theCO_2 molecule. The increase in Rb's charge from 0.72 e^- to 0.86 e^- implies that electron redistribution primarily occurs between the Rb atom and the goldene lattice. This results in strong electrostatic attraction between the positively polarized Rb and the quadrupole moment of CO_2, rather than substantial charge transfer into the molecule. Consequently, the C–O bonds are not perturbed, and CO_2 retains its linear geometry, demonstrating that high adsorption energy does not necessarily correlate with activation.

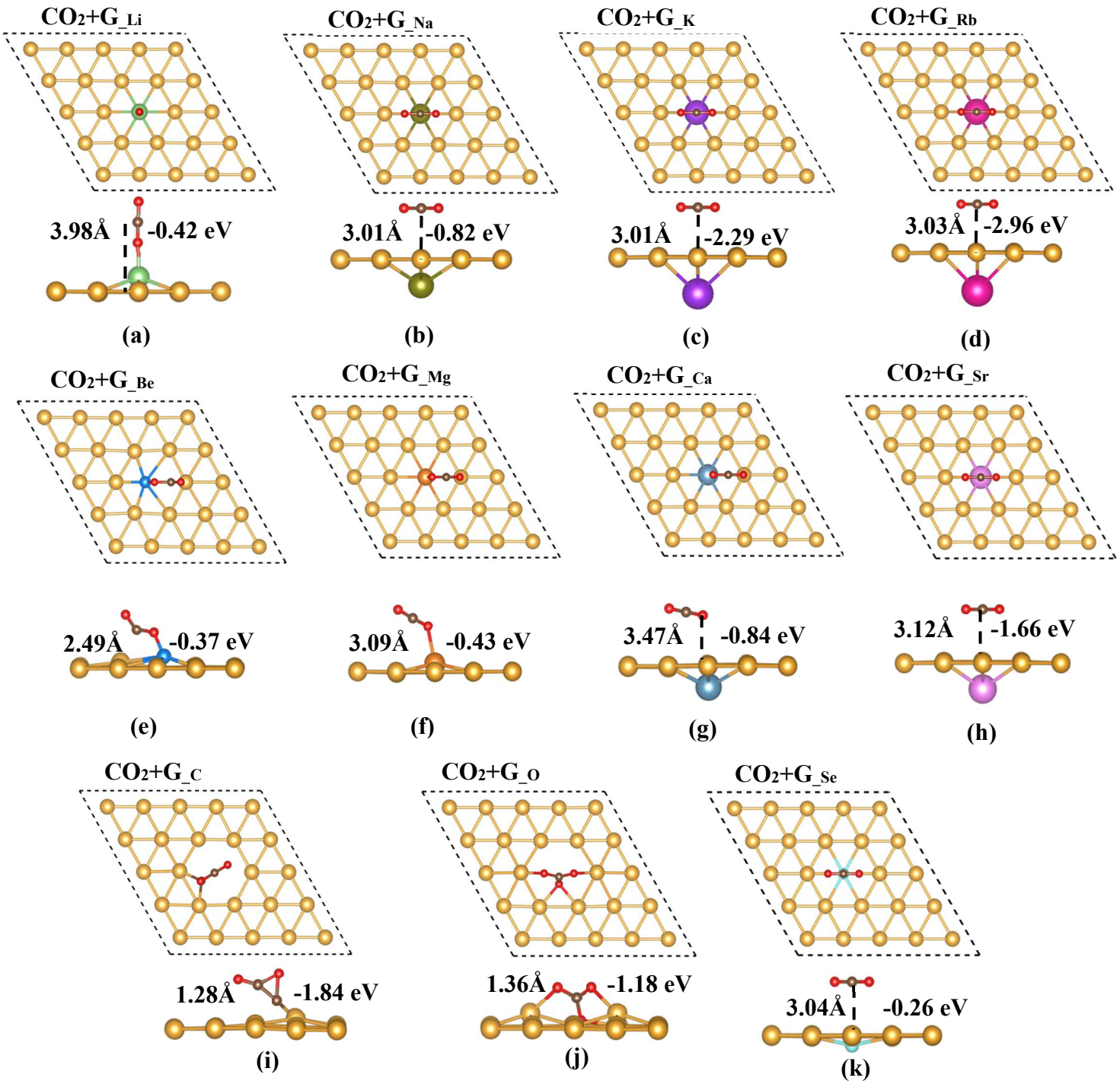

Figure 6 Top and side views of the most stable configurations of CO_2 at (a) G_{Li} (b) G_{Na} (c) G_{K} (d) G_{Rb} (e) G_{Be} (f) G_{Mg} (g) G_{Ca} (h) G_{Sr} (i) G_{C} (j) G_{O} (k) G_{Se} sheets. The maximum adsorption energy for CO_2 is found at the G_{Rb} sheet, while G_{Be}, G_{C}, and G_{O} activate CO_2 for further electrochemical conversion.

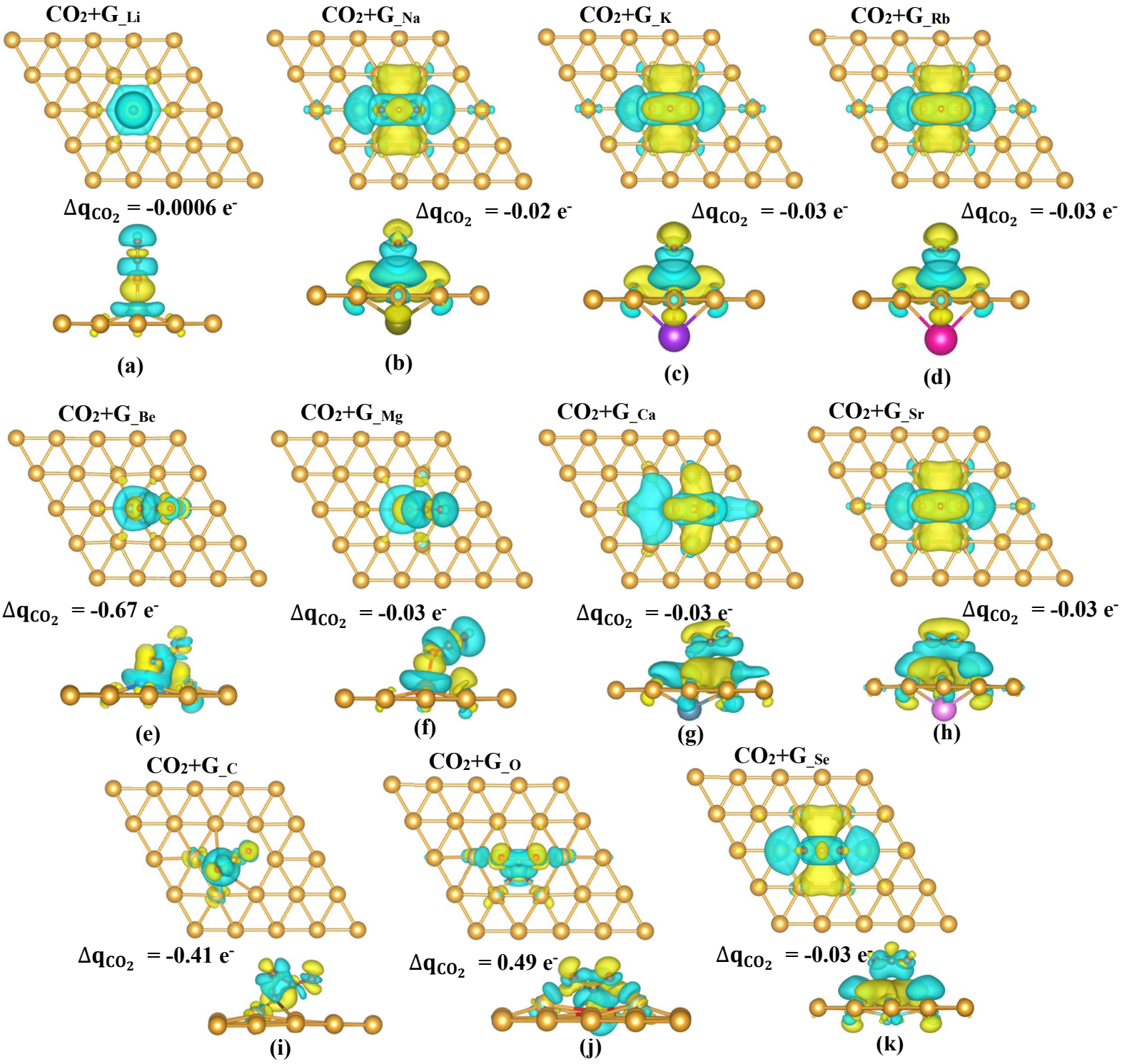

Figure 7 Charge density difference plots of the most stable configurations of CO_2 at (a) G_{Li} (b) G_{Na} (c) G_{K} (d) G_{Rb} (e) G_{Be} (f) G_{Mg} (g) G_{Ca} (h) G_{Sr} (i) G_{C} (j) G_{O} (k) G_{Se} sheets. Oxidation of CO_2 occurs at the G_{O} sheet, while reduction takes place at all other G_{X} sheets.

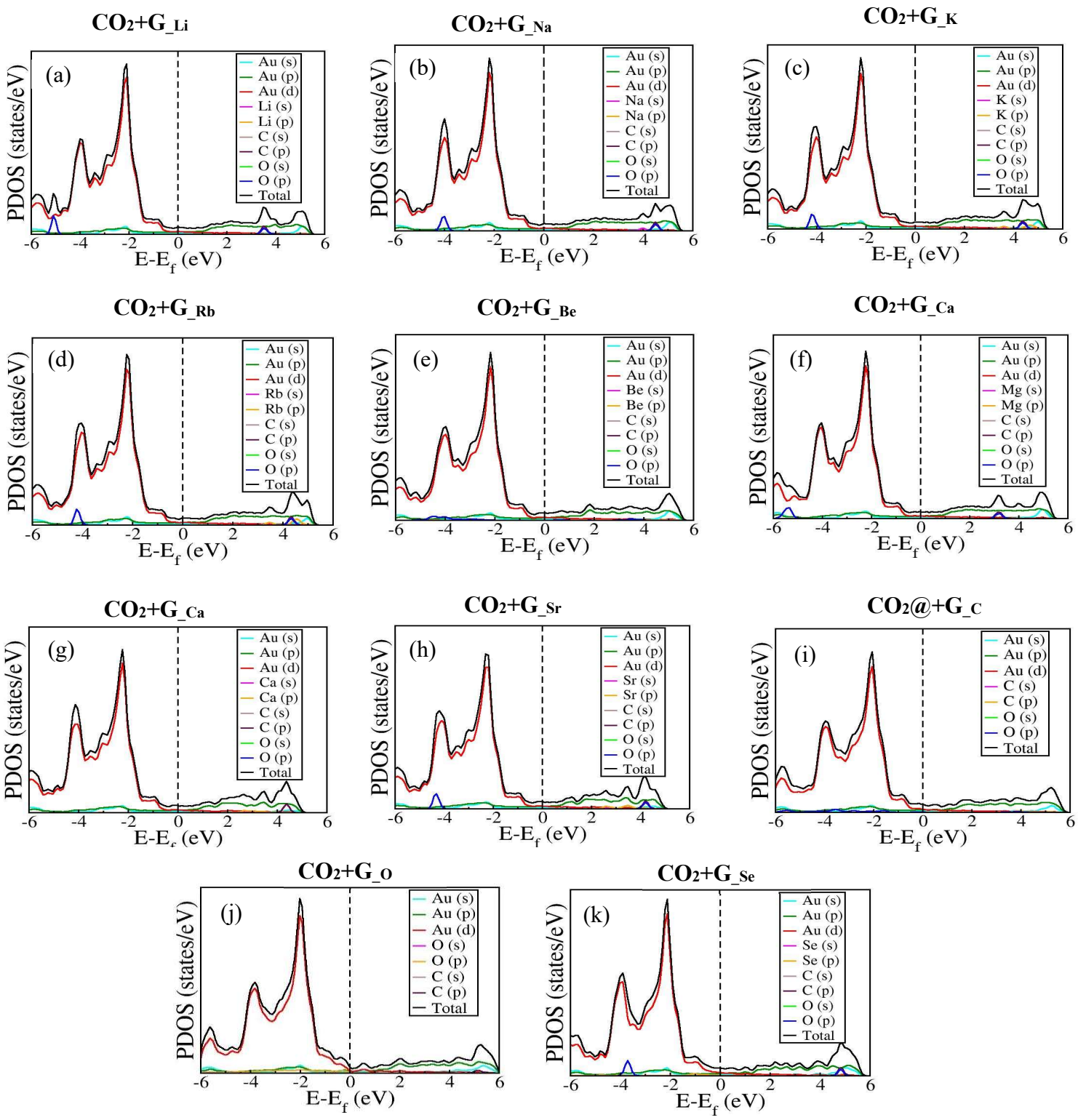

Figure 8 PDOS of the most stable configurations of CO_2 at (a) $G_{\_Li}$, (b) $G_{\_Na}$, (c) $G_{\_K}$, (d) $G_{\_Rb}$ (e) $G_{\_Be}$ (f) $G_{\_Mg}$ (g) $G_{\_Ca}$ (h) $G_{\_Sr}$ (i) $G\text{-}_C$ (j) $G_{\_O}$ (k) $G_{\_Se}$ sheets. In all PDOS, the maximum contribution arises from the d-orbital of the Au atoms.

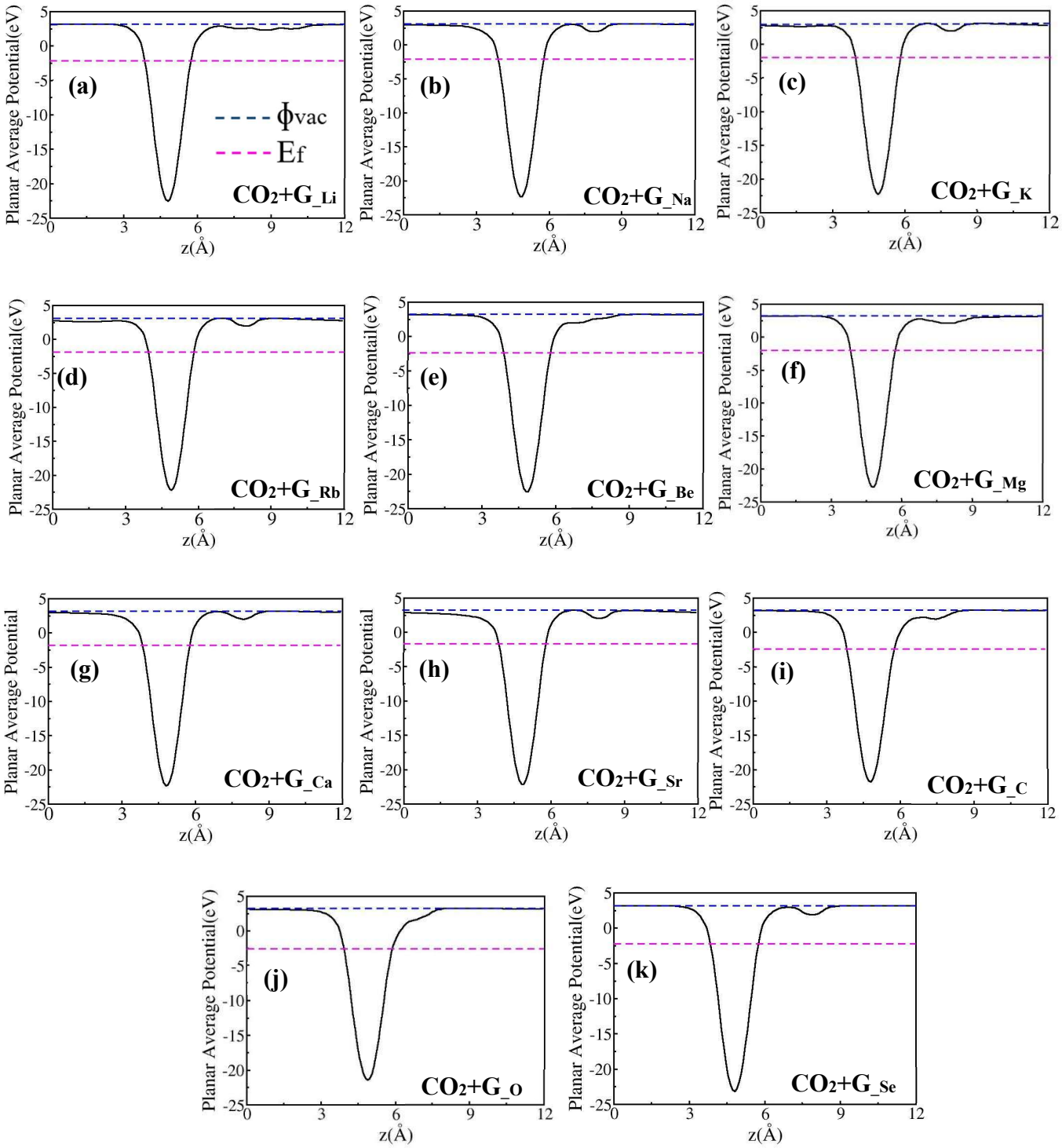

Figure 9. Work function plots of the doped goldene sheets with the most stable configuration of adsorbed CO_2 at (a) $G_{\_Li}$ (b) $G_{\_Na}$ (c) $G_{\_K}$ (d) $G_{\_Rb}$ (e) $G_{\_Be}$ (f) $G_{\_Mg}$ (g) $G_{\_Ca}$ (h) $G_{\_Sr}$ (i) G-C (j) $G_{\_O}$ (k) $G_{\_Se}$ sheets.

4. Phonon analysis

Vibrational and structural analysis of adsorbed CO_2 molecules provides a clear picture of activation on doped goldene sheets. In activated systems such as G_{Be}, G_{C}, and G_{O} doped goldene sheets, the C–O bond lengths are elongated compared to non-activated cases. G_{Be} shows d_3(C–O) = 1.23 Å with a bending angle θ = 136.28°, G_{C} has d_3 = 1.38 Å and θ = 136.79°, and G_{O} has d_3 = 1.27 Å and θ = 122.83°, indicating substantial bond weakening and deviation from linear geometry. A comparison of vibrational frequencies of isolated gas phase CO2 molecule with that if adsorbed form reflects the activation. The bending mode (ν_b) exhibits a blue shift to 696–738 cm^{-1}, while the symmetric (ν_s) and asymmetric (ν_{as}) C–O stretching modes are red-shifted to 1211–1241 cm^{-1} (ν_s) and 1323–1808 cm^{-1} (ν_{as}), consistent with bond weakening. In contrast, non-activated systems such as G_{Li}, G_{Na}, G_{K}, G_{Rb}, G_{Mg}, G_{Ca}, G_{Sr}, and G_{Se} doped goldene sheets retain nearly linear CO_2 geometry (θ ≈ 178–180°) and typical C–O bond lengths (d_3 ≈ 1.16–1.17 Å), with minimal changes in vibrational frequencies (ν_b ≈ 609–640 cm^{-1}, ν_s ≈ 1320–1522 cm^{-1}, ν_{as} ≈ 2239–2350 cm^{-1}). These results demonstrate that CO_2 activation occurs only on G_{Be}, G_{C}, and G_{O} goldene sheets, where C–O bond elongation, molecular bending, and red-shifted stretching frequencies collectively indicate weakening of bonds and electronic perturbation, whereas other dopants primarily induce physisorption or electrostatic binding without activation.

Table 3: A comparsion of calculated vibrational frequencies (bending υ_b, symmetric $\upsilon_{b,}$ and asymmetric υ_{as}) (cm^{-1}) of isolated gas phase CO_2 molecule with that of adsorbed/activated CO_2 molecules at various doped goldene sheets

System	υ_b	υ_s	υ_{as}
Isolated CO_2 molecule	604	1367	2444
CO_2 molecule adsorbed on different sheets			
G_{Li}	631	1333	2377
G_{Na}	638	1320	2349
G_{K}	640	1321	2350
G_{Rb}	638	1320	2348
G_{Be}	696	1241	1808
G_{Mg}	609	1515	2254
G_{Ca}	608	1522	2239
G_{Sr}	639	1321	2350

G_{C}	716	726	1748
G_{O}	738	1211	1323
G_{Se}	638	1320	2349

5. Conclusion

Density functional theory calculations were performed to study CO_2 adsorption and activation at doped (G_{X}) goldene monolayers through detailed analysis of changes in the geometrical and electrical properties. Goldene sheet was doped with AMs (Li, Na, K, Rb), AEMs (Be, Mg, Ca, and Sr), and NMs (C, O, and Se) and binding energies (E_b) of all dopants were calculated, and the G_{Be} sheet was found to form the most robust structure with E_b of -4.73 eV and a Bader charge transfer of 1.95e^- at the doped Be atom. All G_{X} sheets are metallic and thermodynamically favourable with a negative E_b. While some doped configurations exhibit high adsorption energies (E_{ads}), they can maintain a linear CO_2 geometry, demonstrating that strong adsorption does not guarantee molecular activation. The nearly 180° O–C–O bond angle indicates minimal hybridization between the CO_2 molecule and the substrate, characteristic of physisorption. Effective CO_2 activation is linked to significant geometric distortion, particularly bending of the O–C–O angle, which makes these linear configurations catalytically inactive. Therefore, only adsorption sites that promote substantial energy release and structural deformation of CO_2 are considered effective for activation. The CO_2 molecule remains linear after adsorption at AM-doped goldene, with modest adsorption energies (E_{ads}) of -0.42 eV and -0.82 eV at G_{Li} and G_{Na} sheets, respectively, but high adsorption energies of -2.29 eV and -2.96 eV at G_{K} and G_{Rb} sheets, respectively. Non-metal doped goldene sheets, G_{Be}, $G_{C,}$ and G_{O} sheets, effectively activate the CO_2 molecule, where the molecule bends and loses its linearity to connect with the sheets. The weakest interaction of CO_2 was found with the G_{Se} sheet with an E_{a_Se} of only -0.26 eV and low Bader charge transfer of -0.03e^-. The G_{C} sheet with E_{ads} of -1.84 eV and Bader charge transfer to CO_2 of -0.41 is found to be the most appropriate catalyst for the electrochemical reduction of CO_2. Configurations that exhibit strong adsorption and deformation of CO_2 molecules are identified as catalytically active. This study acts as a preliminary screening step, and subsequent calculations are necessary to explore electrochemical conversion pathways.

Acknowledgements

AKM acknowledges the SERB SURE grant (SUR/2022/004935). Via our membership of the UK's HEC Materials Chemistry Consortium, which is funded by EPSRC (EP/X035859), this work made use of the ARCHER2 UK National Supercomputing Service (https://www.archer2.ac.uk). This research work was conducted by the financial support provided by UPES, Dehradun, India.

Conflicts of interest: The authors don't have any conflicts of interest.

Data and code availability: Data is available as Supplementary Information.

Supplementary information: We have given the PDOS and EBS of the unit cell of pristine goldene in Figure S1. Figure S2 represents the EBS of doped goldene. The top and side views of different CO_2 configurations at AM, AEM and NM doped goldene are shown Figures S3, S4 and S5, respectively, while their adsorption energy as well as adsorption heights are given in Table S1. Finally, the EBS of various goldene sheets after CO_2 adsorption are shown in Figure S6.

Ethical approval: Not Applicable.

References

[1] T. M. Ravanchi, S. Sahebdelfar, Catalytic conversions of CO_2 to help mitigate climate change: Recent process developments, Process Safety and Environmental Protection 145 (2021) 172–194.

[2] C. Zhao, L. Wang, L. Huang, N. M. Musyoka, T. Xue, J. Rabeah, Q. Wang, Recent advances in intermediate-temperature CO_2 capture: Materials, technologies and applications, Journal of Energy Chemistry 90 (2024) 435–452.

[3] I. Onyedika, E. Wags, N. Digitemie, Carbon capture and utilization (CCU): A review of emerging applications and challenges, Engineering Science & Technology Journal 5 (2024) 949-961.

[4] P. Miró, M. Audiffred, T. Heine, An atlas of two-dimensional materials, Chemical Society Reviews vol. 43 (2014) 6537–6554.

[5] M. Xu, T. Liang, M. Shi, H. Chen, Graphene-like two-dimensional materials, Chemical Reviews 113 (2013) 3766–3798.

[6] K. R. G. Lim, M. Shekhirev, B. C. Wyatt, B. Anasori, Y. Gogotsi, Z. W. She, Fundamentals of MXene synthesis, Nature Synthesis, 1(2022), 601-614.

[7] W. Choi, N. Choudhary, G. H. Han, J. Park, D. Akinwande, Y. H. Lee, Recent development of two-dimensional transition metal dichalcogenides and their applications. Materials Today, 20(2017), 116-130.

[8] N. Kumar, K. Rangdogia, A. K.Mishra, U. V. Waghmare, C. R. R. Rao, Journal of Solid State Chemistry, 184 (2011), 2902-2908.

[9] P. Kumbhakar, C. C. Gowda, P. L. Mahapatra, M. Mukherjee, K. D. Malviya, M. Chaker, C. S. Tiwary, Emerging 2D metal oxides and their applications, Materials Today, 45 (2021), 142-168.

[10] V. Shanmugam, R. A. Mensah, K. Babu, S. Gawusu, A. Chanda, Y. Tu, O. Das, A review of the synthesis, properties, and applications of 2D materials. Particle & Particle Systems Characterization, 39(2022), 2200031.

[11] Z. Liu, J. Liu, P. Yin, Y. Ge, O. A. Al-Hartomy, A. Al-Ghamdi, H. Zhang, 2D Xenes: optical and optoelectronic properties and applications in photonic devices. Advanced Functional Materials, 32(2022), 2206507.

[12] J. Zhao, H. Liu, Z. Yu, R. Quhe, S. Zhou, Y. Wang, K. Wu, Rise of silicene: A competitive 2D material, Progress in Materials Science, 83 (2016), 24-151.

[13] S. S. Dongre, C. Hunsur Ravikumar, R. G. Balakrishna, Review on 2D arsenene and antimonene: emerging materials for energy, electronic and biological applications, Advanced Materials Interfaces, 9(2022), 2200442.

[14] F. F. Zhu, W. J. Chen, Y. Xu, C. L. Gao, D. D. Guan, C. H. Liu, J. F. Jia, Epitaxial growth of two-dimensional stanene, Nature materials, 14(2015), 1020-1025.

[15] W. Wu, G. Qiu, Y. Wang, R. Wang, P. Ye, Tellurene: its physical properties, scalable nanomanufacturing, and device applications, Chemical Society Reviews vol. 47 (2018) 7203–7212.

[16] F. Yang, A. O. Elnabawy, R. Schimmenti, P. Song, J. Wang, Z. Peng, W. Xu, Bismuthene for highly efficient carbon dioxide electroreduction reaction. Nature Communications, 11(2020), 1088.

[17] T. Wang, H. Wang, Z. Kou, W. Liang, X. Luo, F. Verpoort, H. Zhang, Xenes as an emerging 2D monoelemental family: fundamental electrochemistry and energy applications. Advanced Functional Materials, 30(2020), 2002885.

[18] N. Martín, N. Tagmatarchis, Q. H. Wang, X. Zhang, Chemical Functionalization of 2D Materials. Chemistry - A European Journal 26 (2020) 6292–6295.

[19] K. Kumar, N. H. De Leeuw, J. Adam, A. K. Mishra, Strain-Induced Bandgap Engineering in 2D ψ-Graphene Materials: A First-Principles Study, Beilstein Journal of Nanotechnology, 15(2024) 1440-1452.

[20] M. Manzoor, K. Kumar, A. K. Mishra, B. A. Al-Asbahi, R. Sharma, Effect of strain on opto-electronic and thermoelectric properties of 2D SiH monolayer for solar cell and renewable energy applications: A first-principles study, Solid State Commun 386, (2024) 115527.

[21] Y. Zhou, X. Lin, Effects of interstitial dopings of 3d transition metal atoms on antimonene: A first-principles study, Appl Surf Sci 458 (2018), 572–579.

[22] Y. Sun, Y. Zhao, Z. Liang, H. Lin, Z. Ren, Z. Yao, D. Zhu, Reversible potassium-ion alloying storage in crystalline silicene, Chemical Engineering Journal, 435 (2022), 134961.

[23] E. J. Jelmy, N. Thomas, D. T. Mathew, J. Louis, N. T. Padmanabhan, V. Kumaravel, S. C. Pillai, Impact of structure, doping and defect-engineering in 2D materials on CO_2 capture and conversion, Reaction Chemistry & Engineering, 6(2021), 1701-1738.

[24] Y. Li, Q. Sun, Recent advances in breaking scaling relations for effective electrochemical conversion of CO_2, Advanced Energy Materials, 6(2016), 1600463.

[25] E. Olsson, G. Chai, M. Dove, Q. Cai, Adsorption and migration of alkali metals (Li, Na, and K) on pristine and defective graphene surfaces, Nanoscale, 11(2019), 5274-5284.

[26] M. Sun, W. Tang, Q. Ren, S. Wang, Y. Du, Y. Zhang, First-principles study of the alkali earth metal atoms adsorption on graphene, Applied Surface Science, 356 (2015), 668-673.

[27] A. V. Krasheninnikov, P. O. Lehtinen, A. S. Foster, P. Pyykkö, R. M. Nieminen, Embedding transition-metal atoms in graphene: structure, bonding, and magnetism. Physical review letters, 102(2019), 126807.

[28] Y. Tang, Z. Yang, X. Dai, D. Ma, Z. Fu, Formation, stabilities, and electronic and catalytic performance of platinum catalyst supported on non-metal-doped graphene, Journal of Physical Chemistry C 117 (2013), 5258–5268.

[29] M. Lalitha, Y. Nataraj, S. Lakshmipathi, Calcium decorated and doped phosphorene for gas adsorption. Appl Surf Sci 377 (2016), 311–323.

[30] A. Ebrahimi, M. Izadyar, Li-decorated black phosphorene: A promising platform for gas molecule adsorption. Int J Quantum Chem 124, (2024) e27427.

[31] J. Zhu, A. Chroneos, U. Schwingenschlögl, CO_2 capture by Li-functionalized silicene. Physica Status Solidi - Rapid Research Letters 10, 458–461 (2016).

[32] V. Arefi, A. Horri, M. B. Tavakoli, Transport properties of Na-decorated borophene under CO/CO_2 adsorption. Comput Theor Chem, 1197 (2021) 113159.

[33] S. L. Hou, J. Dong, X. Y. Zhao, X. S. Li, F. Y. Ren, J. Zhao, B. Zhao, Thermocatalytic conversion of CO2 to valuable products activated by noble-metal-free metal-organic frameworks, Angewandte Chemie International Edition, 62(2023), e202305213.

[34] Y. Tang, Z. Yang, X. Dai, D. Ma, Z. Fu, Formation, stabilities, and electronic and catalytic performance of platinum catalyst supported on non-metal-doped graphene, Journal of Physical Chemistry C 117 (2013)5258–5268.

[35] M. D. Hughes, Y. J. Xu, P. Jenkins, P. McMorn, P. Landon, D. I. Enache, C. J. Kiely, Tunable gold catalysts for selective hydrocarbon oxidation under mild conditions, Nature, 437(2005), 1132-1135.

[36] Y. Mikami, A. Dhakshinamoorthy, M. Alvaro, H. García, Catalytic activity of unsupported gold nanoparticles. Catalysis Science and Technology, 3 (2013) 58–69.

[37] L/ M. Yang, M. Dornfeld, T. Frauenheim, E. Ganz, Glitter in a 2D monolayer. Physical Chemistry Chemical Physics, 17 (2015) 26036–26042.

[38] X. Wang, C. Wang, C. Chen, H. Duan, K. Du, Free-standing Monatomic Thick Two-dimensional Gold. Nano Lett 19 (2019), 4560–4566.

[39] S. Kashiwaya, Y. Shi, J. Lu, D. Sangiovanni, M. Andersson, J. Rosen, L. Hultman, Goldene: Free-standing Single-atom-thick Sheets of Gold (2023).

[40] Y. Shi, S. Kashiwaya, J. Lu, M. Dahlqvist, D. G. Sangiovanni, V. Rogoz, L. Hultman, Synthesis of Ti4Au3C3 and its derivative trilayer goldene through chemical exfoliation. *Science Advances*, 11(2025), eadt7999.

[41] S. Kashiwaya, Y. Shi, J. Lu, D. G. Sangiovanni, G. Greczynski, M. Magnuson, L. Hultman, Synthesis of goldene comprising single-atom layer gold. *Nature Synthesis*, 3(2024), 744-751.

[42] K. Kumar, N. H. de Leeuw, J. Adam, A. K. Mishra, Mechanistic insights into CO2 activation on pristine, vacancy-containing and doped goldene: a single-atom layer of gold. *Physical Chemistry Chemical Physics*, 47(2024) 29420-29431.

[43] S. Ullah, L. Li, Y. Wang, X. Yang, M. Tang, Y. Xiang, Q. Yang, Controllable p-type doping of 2D MoS 2 via Sodium intercalation for optoelectronics. *Journal of Materials Chemistry C*, 11(2023), 3386-3394.

[44] D. Marchiani, N. Jimenez-Arevalo, M. Sbroscia, C. Cardoso, D. Prezzi, C. Mariani, R. Frisenda, Spatial mapping of potassium diffusion and intercalation in few-layer graphene studied by ultra-high vacuum micro-Raman spectroscopy. *Nano Energy*, 142 (2025), 111274.

[45] J. Chapman, Y. Su, C. A. Howard, D. Kundys, A. N. Grigorenko, F. Guinea, R. Nair, Superconductivity in Ca-doped graphene laminates. *Scientific reports*, 6(2016), 23254.

[46] P Giannozzi, O. Andreussi, T. Brumme, O. Bunau, M. B. Nardelli, M. Calandra, R. Car, C. Cavazzoni, D. Ceresoli, M. Cococcioni, N. Colonna, I. Carnimeo, A. Dal Corso, S. De Gironcoli, P. Delugas, R. A. Distasio, A. Ferretti, A. Floris, G. Fratesi, G. Fugallo, R. Gebauer, U. Gerstmann, F. Giustino, T. Gorni, J. Jia, M. Kawamura, H. Y. Ko, A. Kokalj, E. Küçükbenli, M. Lazzeri, M. Marsili, N. Marzari, F. Mauri, N. L. Nguyen, H. V. Nguyen, A. Otero-De-La-Roza, L. Paulatto, S. Poncé, D. Rocca, R. Sabatini, B. Santra, M. Schlipf, A. P. Seitsonen, A. Smogunov, I. Timrov, T.

Thonhauser, P. Umari, N. Vast, X. Wu, S. Baroni, Advanced Capabilities for Materials Modelling with Quantum ESPRESSO, Journal of Physics: Condensed Matter, 29 (2017) 465901.

[47] M. Orio, D. A. Pantazis, F. Neese, Density functional theory. *Photosynthesis Research,* 102 (2009) 443–453.

[48] J. P. Perdew, K. Burke, M. Ernzerhof, generalized gradient approximation made simple, Physical Review Letters, 77(1996), 3865.

[49] M. Ropo, K. Kokko, L. Vitos, Assessing the Perdew-Burke-Ernzerhof exchange-correlation density functional revised for metallic bulk and surface systems. Physical Review B—Condensed Matter and Materials Physics, 77(2008), 195445.

[50] A. D. Corso, Pseudopotentials periodic table: From H to Pu. *Comput Mater Sci* 95 (2014), 337–350.

[51] G. Kresse, D. Joubert, from ultrasoft pseudopotentials to the projector augmented-wave method. Physical Review B, 59(1999), 1758.

[52] J. Moellmann, S. Grimme, DFT-D3 study of some molecular crystals. Journal of Physical Chemistry C 118 (2014), 7615–7621.

[53] G. Henkelman, A. Arnaldsson, H. A. Jónsson, Fast and robust algorithm for Bader decomposition of charge density. Comput Mater Sci 36 (2006), 354–360.

[54] M. N. Groves, A. S. W. Chan, C. Malardier-Jugroot, M. Jugroot, Improving platinum catalyst binding energy to graphene through nitrogen doping. *Chemical Physics Letters*, 481(2009), 214-219.

[55] M. Topsakal, E. Aktürk, S. J. P. R. B. Ciraci, First-principles study of two-and one-dimensional honeycomb structures of boron nitride. *Physical Review B—Condensed Matter and Materials Physics*, 79(2009), 115442.

[56] B. Zhu, L. Zhang, D. Xu, B. Cheng, J. Yu, Adsorption investigation of CO2 on g-C3N4 surface by DFT calculation. *Journal of CO2 Utilization*, 21(2017), 327-335.

[57] S. De Waele, K. Lejaeghere, M. Sluydts, S. Cottenier, Error estimates for density-functional theory predictions of surface energy and work function. *Physical Review B*, 94(2016), 235418.